



RESEARCH ARTICLE SUMMARY

SPATIAL OMICS

Spatially resolved single-cell translomics at molecular resolution

Hu Zeng[†], Jiahao Huang[†], Jingyi Ren[†], Connie Kangni Wang, Zefang Tang, Haowen Zhou, Yiming Zhou, Hailing Shi, Abhishek Aditham, Xin Sui, Hongyu Chen, Jennifer A. Lo, Xiao Wang*

INTRODUCTION: Cellular proteins are the final products of gene expression that execute cellular functions. To understand translational gene regulation, it is crucial to measure protein synthesis at single-cell and spatial resolution. Current ribosome profiling methods achieve transcriptome-wide translational analysis but lack spatial context. By contrast, imaging-based methods preserve spatial information but are not multiplexed. A scalable method for single-cell and spatially resolved profiling of protein synthesis is still needed.

RATIONALE: We introduce ribosome-bound mRNA mapping (RIBOmap), a highly multiplexed method for spatial charting of protein synthesis at single-cell and subcellular resolution. RIBOmap employs a targeted-sequencing strategy that selectively detects ribosome-bound mRNAs through a specific design of tri-probes. The tri-probe set consists of a splint DNA probe hybridized to ribosomal RNA and a pair

of padlock and primer probes hybridized to mRNAs, which together produce DNA amplicons with gene-unique barcodes through *in situ* amplification. These DNA amplicons are then embedded in a polyacrylamide hydrogel matrix and the gene-unique barcodes are read out through *in situ* sequencing. We validated the specificity of RIBOmap through the use of noncoding RNAs, translation inhibitor, *in vitro* transcribed mRNAs, and comparison with established ribosome profiling technology.

RESULTS: We applied RIBOmap to HeLa cells for a 981-gene multiplexed experiment and designed a multimodal RIBOmap imaging experiment to capture the cell-cycle phase and subcellular organelles. The results revealed cell-cycle-dependent translation and subcellular localized mRNA translation in HeLa cells. We further applied RIBOmap to intact mouse brain tissue, measuring the translation of 5413 genes simultaneously. Leveraging the single-cell and

spatial resolutions of RIBOmap, we generate a single-cell spatial map of the mouse brain. Comparing the spatial translomics generated by RIBOmap with spatial transcriptomics, we uncovered cell type-specific and brain region-specific translational regulation.

CONCLUSION: RIBOmap presents a new spatially resolved single-cell translomics technology, accelerating our understanding of protein synthesis in the context of subcellular architecture, cell types, and tissue anatomy. The pairwise spatial translomic and transcriptomic mapping enabled us to systematically identify cell type- and tissue-region-specific translational regulation, paving the way for uncovering novel posttranscriptional gene regulation principles and mechanisms that shape the proteome for cellular and tissue functions. RIBOmap bypasses complicated polysome isolation steps and genetic manipulation, making it promising for studies in post hoc human tissue and disease samples. We anticipate that integrating RIBOmap with other imaging-based measurements will enable spatial multiomics mapping for a comprehensive understanding of biological systems. ■

The list of author affiliations is available in the full article.

*Corresponding author. Email: xwangx@mit.edu

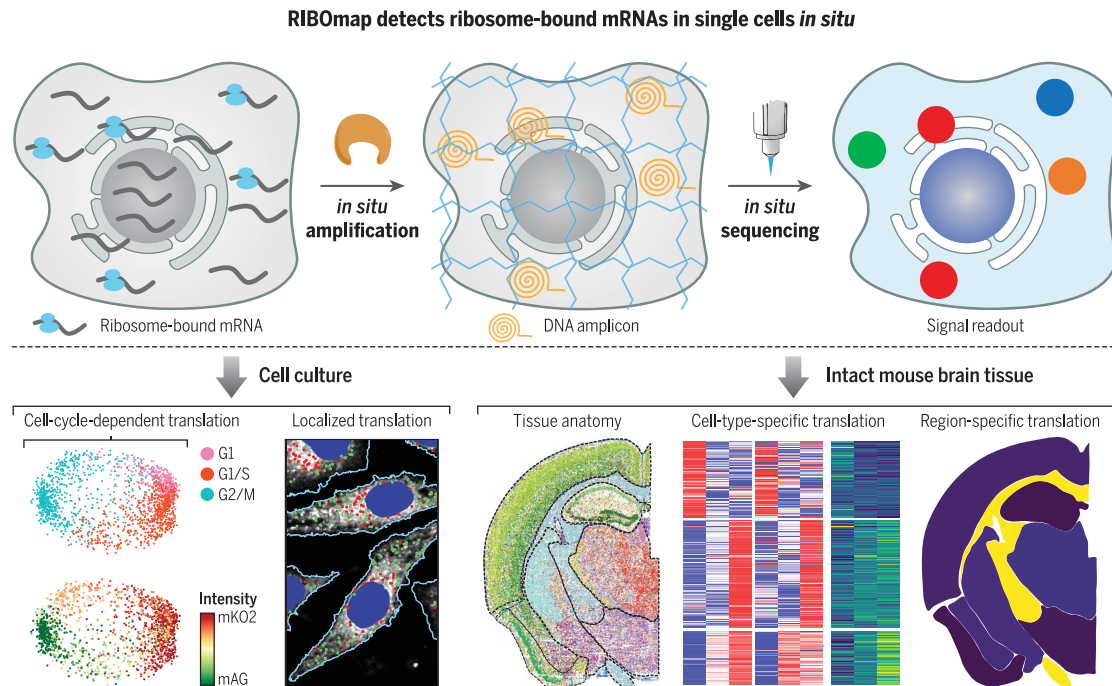
†These authors contributed equally to this work.

Cite this article as: H. Zeng et al., *Science* **380**, eadd3067 (2023). DOI: [10.1126/science.add3067](https://doi.org/10.1126/science.add3067)

S READ THE FULL ARTICLE AT
<https://doi.org/10.1126/science.add3067>

RIBOmap for spatial translomics imaging

RIBOmap is a three-dimensional (3D) *in situ* profiling technology designed to selectively measure ribosome-bound mRNAs, providing spatially resolved single-cell translomic analysis at molecular resolution. In cell culture, RIBOmap uncovers cell-cycle-dependent and subcellular localized translation. When applied to intact mouse brain tissue, RIBOmap generates spatial tissue atlases and reveals cell-type-specific and tissue region-specific translational regulation.



RESEARCH ARTICLE

SPATIAL OMICS

Spatially resolved single-cell translomics at molecular resolution

Hu Zeng^{1,2†}, Jiahao Huang^{1,2†}, Jingyi Ren^{1,2†}, Connie Kangni Wang², Zefang Tang^{1,2}, Haowen Zhou², Yiming Zhou^{1,2,3}, Hailing Shi^{1,2}, Abhishek Aditham^{2,4}, Xin Sui^{1,2}, Hongyu Chen^{1,2}, Jennifer A. Lo², Xiao Wang^{1,2*}

The precise control of messenger RNA (mRNA) translation is a crucial step in posttranscriptional gene regulation of cellular physiology. However, it remains a challenge to systematically study mRNA translation at the transcriptomic scale with spatial and single-cell resolution. Here, we report the development of ribosome-bound mRNA mapping (RIBOmap), a highly multiplexed three-dimensional *in situ* profiling method to detect cellular translome. RIBOmap profiling of 981 genes in HeLa cells revealed cell cycle-dependent translational control and colocalized translation of functional gene modules. We mapped 5413 genes in mouse brain tissues, yielding spatially resolved single-cell translomic profiles for 119,173 cells and revealing cell type-specific and brain region-specific translational regulation, including translation remodeling during oligodendrocyte maturation. Our method detected widespread patterns of localized translation in neuronal and glial cells in intact brain tissue networks.

Measuring genome-wide protein synthesis patterns with single-cell and spatial resolution can help us understand translational regulation in heterogeneous cell types and states. Although large-scale single-cell and spatially resolved proteome profiling remains challenging (1), past research has focused on mapping mRNA levels to infer the corresponding protein abundances in single cells. However, numerous studies have revealed poor correlation between mRNA and protein levels (2–5), as gene regulation is achieved at both transcriptional and translational levels. Moreover, many genes undergo signal-dependent and subcellular-localized translation (6). Therefore, we need scalable single-cell and spatially resolved profiling of protein synthesis for a comprehensive understanding of gene expression and translational regulation.

Existing bulk and single-cell ribosome profiling methods have enabled us to analyze protein translation at the transcriptome scale (7–12) but cannot preserve spatial information. Current imaging-based methods that can trace mRNA translation with their physical coordinates (13–19) are limited to low gene throughput. Therefore, it remains challenging to achieve highly multiplexed spatial ribosome profiling in single cells with subcellular resolution. To

fill this gap, we developed a three-dimensional (3D) *in situ* ribosome-bound mRNA mapping method (RIBOmap) for highly multiplexed characterization of protein synthesis with single-cell and subcellular resolutions.

RIBOmap design and validation

RIBOmap is built upon a targeted-sequencing strategy in which a specific design of tri-probes selectively detects and amplifies ribosome-bound mRNAs (Fig. 1A and fig. S1A). The RIBOmap tri-probe set includes: (i) a splint DNA probe that hybridizes to ribosomal RNAs (rRNAs) and serves as the splint to circularize the adjacent padlock probe; (ii) a padlock probe that targets specific mRNA species of interest and encodes a gene-unique barcode; (iii) a primer probe that targets the mRNA site adjacent to the one targeted by the padlock probe and serves as the primer for rolling circle amplification resulting in a DNA nanoball (amplicon). DNA amplicon signals are only produced when all three probes are present in proximity (Fig. 1, B and C). The gene-unique barcodes in the DNA amplicons are then decoded through *in situ* sequencing with error-reduction by dynamic annealing and ligation (Fig. 1A) (20). We also tested an alternative RIBOmap workflow that uses primary antibodies of ribosomal proteins (RPS3, RPL4) and splint-conjugated protein A/G to target ribosomes, which demonstrated a much lower signal-to-noise ratio (SNR) than that of the rRNA targeting strategy (fig. S1, B to G). Thus, we proceeded with the rRNA targeting strategy in the following studies.

To confirm that RIBOmap specifically targets ribosome-bound mRNAs, we designed

four experiments. First, RIBOmap and previously reported STARmap RNA imaging (20) were used to detect protein-encoding *ACTB* mRNA and two negative controls of noncoding RNAs (Fig. 2A and table S1). As expected, RIBOmap only detected cytoplasmic *ACTB* mRNAs whereas STARmap detected both *ACTB* mRNA and the noncoding RNAs (Fig. 2, B and C and fig. S2). Second, RIBOmap specificity was validated using Harringtonine, a translation inhibitor that traps translation-initiating ribosomes at the start codon (21) (Fig. 2D). After Harringtonine treatment, there was a significant decrease in RIBOmap signal intensity using probes targeting 115 or 405 nucleotides (nt) downstream of the start codon, whereas there was minimal decrease in the signal generated by the probe targeting the -16 nt from the start codon (Fig. 2, E to G). Third, we used synthetic *in vitro* transcribed (IVT) mRNAs and lipid-mediated transfection (Fig. 2H). Our data demonstrated that STARmap could detect both small puncta corresponding to free cytosolic mRNAs and larger intracellular granules corresponding to lipid transfection vesicles containing many copies of nontranslating mRNAs, whereas RIBOmap signals were depleted in lipid transfection vesicles (Fig. 2, I and J), indicating that RIBOmap does not detect nontranslating mRNAs. Finally, we validated RIBOmap by comparing it with RiboLace, an established ribosome profiling technology (22). RIBOmap successfully detected differentially translated mRNAs in starved versus control human MCF7 cells, which is consistent with the reported RiboLace and proteomics measurements (22) (fig. S3). Together, these results demonstrate the specificity of RIBOmap in detecting ribosome-bound mRNAs.

Multiplexed RIBOmap in cultured cells

After benchmarking the SNR and specificity of RIBOmap, we performed a highly multiplexed 981-gene RIBOmap experiment in HeLa cells (Fig. 3A). The 981 genes represent a curated list composed of cell-cycle gene markers, genes with diverse subcellular RNA patterns, and genes of varying RNA stabilities (23–26) (table S2). We designed a multimodal RIBOmap imaging experiment that further incorporated the information on cell-cycle stages and subcellular organelles: (i) the cell-cycle phase of each cell was captured by the fluorescent ubiquitination-based cell cycle indicators (Fucci) (27, 28); (ii) ribosome-bound mRNAs (981 genes) were *in situ* sequenced; (iii) finally, nuclei, endoplasmic reticulum, and cell shapes were stained and imaged (Fig. 3B). We also conducted a paired STARmap experiment for comparison (Fig. 3A). In total, RIBOmap and STARmap sequenced 1813 and 1757 cells, respectively (fig. S4A). The median distance between each read and its nearest neighbor in

¹Department of Chemistry, Massachusetts Institute of Technology, Cambridge, MA 02139, USA. ²Broad Institute of MIT and Harvard, Cambridge, MA 02142, USA. ³Center for Psychiatric Research, Broad Institute of MIT and Harvard, Cambridge, MA 02142, USA. ⁴Department of Biological Engineering, Massachusetts Institute of Technology, Cambridge, MA 02139, USA.

*Corresponding author. Email: xwangx@mit.edu

†These authors contributed equally to this work.

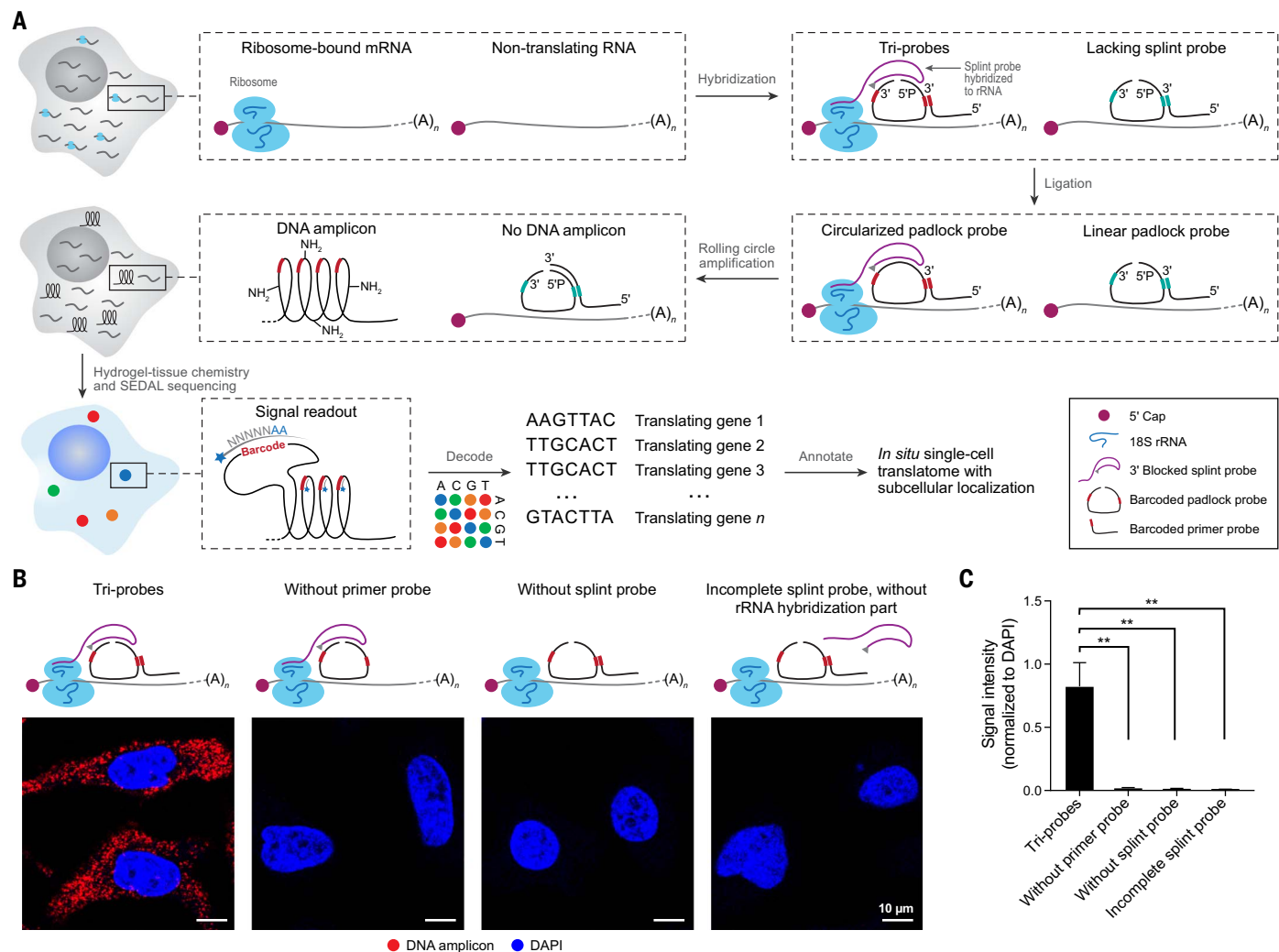


Fig. 1. RIBOmap for in situ profiling of mRNA translation at subcellular resolution. (A) Schematic of RIBOmap. After the sample is prepared, a paired barcoded padlock probe and primer probe are hybridized to a targeted intracellular RNA, and the splint probe is hybridized to 18S rRNA of ribosomes. The splint probe is used as a template for the proximity ligation to circularize the padlock probe. The intact padlock probe can then be amplified to generate amine-modified DNA amplicons in situ. Next, these DNA amplicons are copolymerized into hydrogel through tissue-hydrogel chemistry for in situ sequencing. The gene-unique barcode

sequence (red) in the cDNA amplicons can then be read out through cyclic in situ sequencing. (B) Tri-probe strategy. (Left) Fluorescent images of tri-probe condition show the RIBOmap signal of ACTB mRNA in HeLa cells. (Middle) Fluorescent images of negative control samples without the primer or splint probe show minimum DNA amplicon signal. (Right) Fluorescent images of the control sample using a splint probe without the rRNA hybridization sequence show minimal DNA amplicon signal. (C) Quantification of the DNA amplicon signal intensity shown in (B). Error bars, standard deviation. $n = 3$ images per condition. Student's t -test, ** $P < 0.01$.

3D was 0.69 μm for RIBOmap and 0.61 μm for STARmap (fig. S4, B and C), indicating that both techniques have high spatial resolution. To assess the reliability of RIBOmap in multiplexed experiments, we calculated the correlation between the RIBOmap results for 981 genes with published HeLa proteome and ribosome profiling datasets (26, 29, 30). The results showed that the correlation between RIBOmap and the proteome dataset is comparable to that between the ribosome profiling dataset and the proteome dataset (fig. S4D). Additionally, the correlation between RIBOmap and the two ribosome profiling datasets is comparable to the correlation between the two ribosome profiling datasets (fig. S4E).

Next, we evaluated whether RIBOmap can decipher cell cycle-dependent mRNA translation. The results showed that the G1, G1/S, and G2/M cell cycle phases identified from both RIBOmap and STARmap datasets agreed with the expected cell cycle-dependent patterns of FUCCI protein fluorescence (Fig. 3C and fig. S5), demonstrating the accuracy of RIBOmap in delineating cell states. We then identified the differentially expressed genes (DEGs) across cell cycle phases using RIBOmap and STARmap data (fig. S6, A and B, and table S3). Most of the RIBOmap DEGs overlapped with known cell cycle-dependent genes (31) (fig. S6C). We also identified DEGs detected in RIBOmap but not in STARmap (fig. S6D). One example is *NOL6*

(nucleolar protein 6), whose translation was significantly decreased from the G1 phase to the G2/M phase as detected by both RIBOmap and ribosome profiling (32), but whose overall RNA level showed little change across cell cycle phases as detected by STARmap and RNA-seq (fig. S6, E to G).

Next, to leverage the single-cell resolution in our dataset, we performed gene-expression co-variation analysis and identified five coregulated translation modules (RTMs) with substantial intramodule correlation, each with enrichment of distinct functional pathways (RTMs 1 to 5, Fig. 3D, fig. S7, A to E, and table S4). RTM 3 and RTM 5 are enriched for G2/M and G1/S cell cycle marker genes, respectively (Fig. 3D,

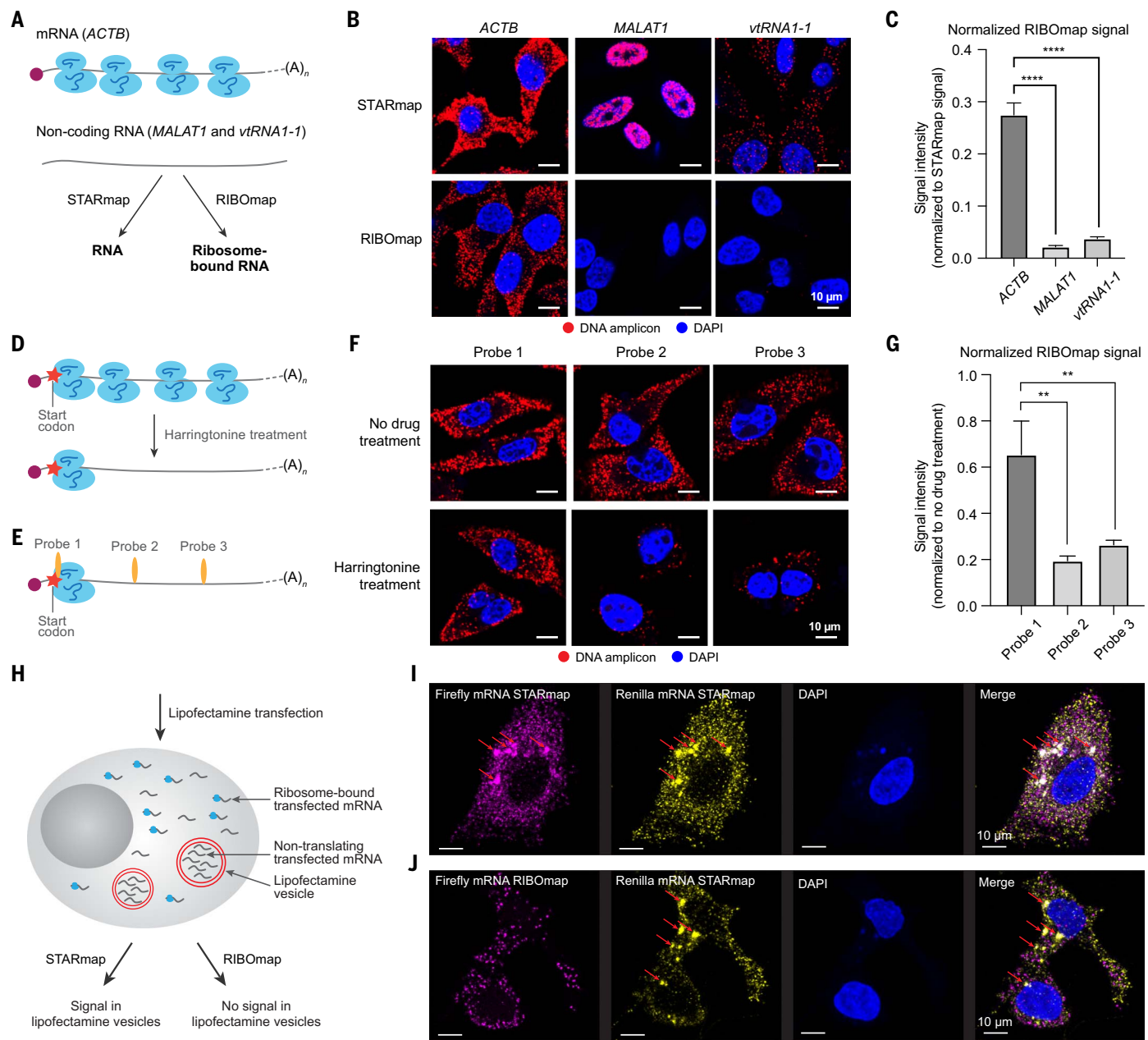


Fig. 2. RIBOmap specificity validation. (A) Schematic of RIBOmap signal verification by targeting mRNA (*ACTB*) and noncoding RNA (*MALAT1* and *vtRNA1-1*). (B) Fluorescent images show RNA detection results by STARmap and translating RNA detection results by RIBOmap. (C) Quantification of the DNA amplicon signal intensity shown in (B). Error bars, standard deviation. $n = 5$ images per condition. Student's *t*-test, *** $P < 0.0001$. (D) Schematic of translational regulation by Harringtonine. (E) Three pairs of padlock and primer probes targeting different sites of *ACTB* mRNA. (F) Fluorescent images show the RIBOmap signal of 3 sets of probes targeted to different regions of *ACTB* mRNA.

in HeLa cells before and after Harringtonine treatment. (G) Quantification of the RIBOmap signal intensity shown in (F). Error bars, standard deviation. $n = 3$ images per condition. Student's *t*-test, ** $P < 0.01$. (H) Schematic representation of RIBOmap signal verification using transfected IVT mRNAs. (I) Fluorescent images show RNA detection of transfected Firefly mRNA and Renilla mRNA by STARmap. The lipofectamine vesicles are labeled by red arrows. (J) Fluorescent images show RNA detection results of transfected Renilla mRNA by STARmap and translating RNA detection of transfected Firefly mRNA by RIBOmap. The lipofectamine vesicles are labeled as in (I).

right), and are negatively correlated (fig. S7F). Moreover, RTM 2 contains genes encoding protein translation machineries (fig. S7D); these genes show a positive correlation with RTM 5 (G1/S marker genes) and a negative correlation with RTM 3 (G2/M marker genes) (fig. S7G). This observation suggests that the

protein translation machinery is up-regulated in the G1/S phase to support the demand for protein products as cells enlarge and subcellular organelles are replicated.

Subcellular localized translation has implications for signal transduction and proteome organization (6). Using RIBOmap results, we

identified five colocalized translation modules (LTMs) with highly correlated subcellular spatial organizations and distinct functional enrichment (LTMs 1 to 5, Fig. 3, E to G, fig. S8, A to C, and table S4). Among them, LTMs 2, 4, and 5 are enriched with a membrane protein and secretion pathway (Fig. 3, F and G and

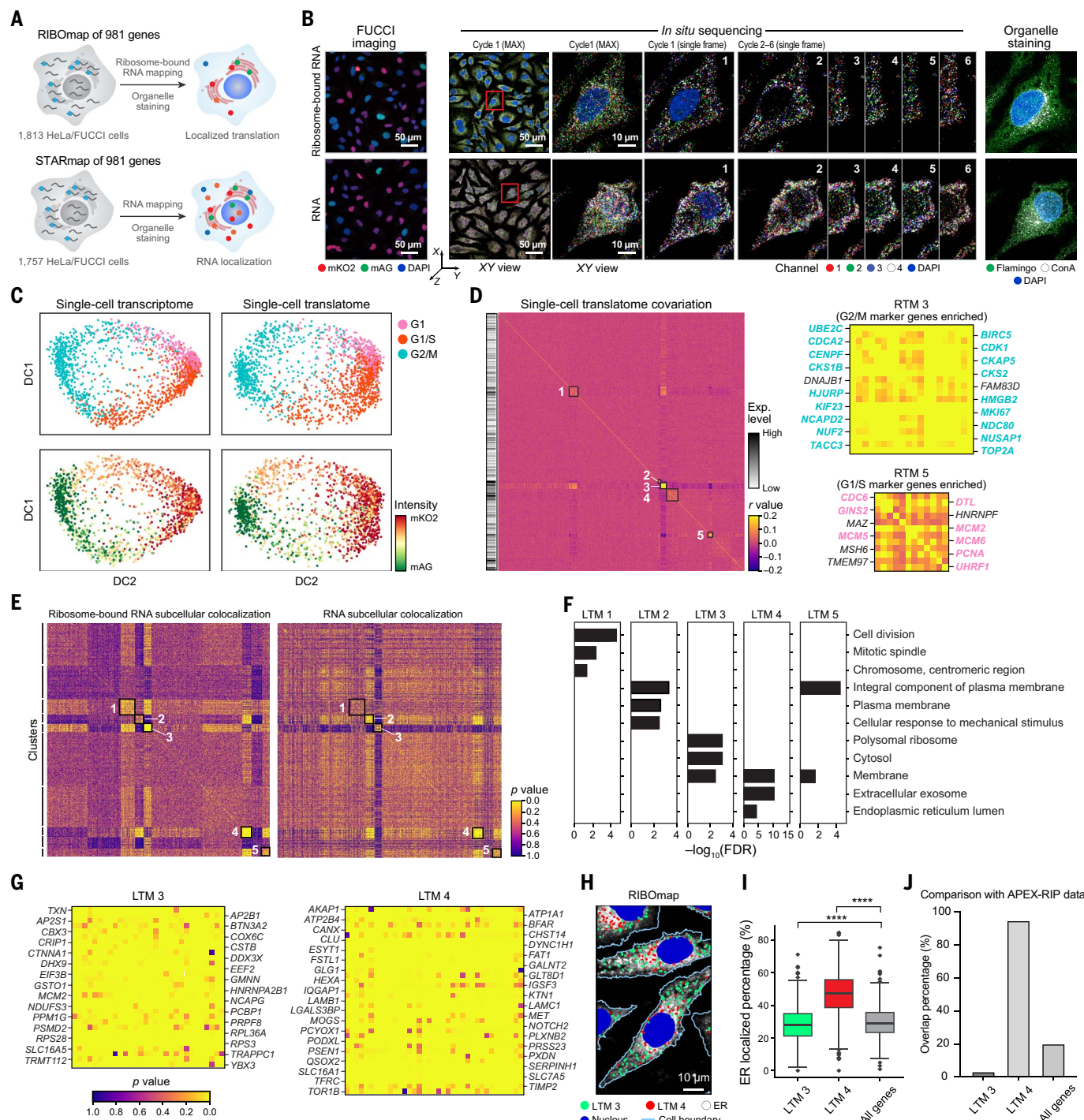


Fig. 3. RIBOmap simultaneously measures the subcellular translation of 981 genes in human HeLa cells. **(A)** Schematic of RIBOmap detection in HeLa FUCCI cells to measure localized mRNA translation. **(B)** Representative images showing the sequential mapping of FUCCI fluorescence signal, cDNA amplicons, and organelle staining in the same HeLa cell sample. (Left) the FUCCI cell fluorescence imaging results for RIBOmap (upper) and STARmap (bottom). (Middle) Representative images showing the maximum intensity projections (MAX) of the first sequencing cycle with zoom-in views of a representative cell and single-frame views of the representative cell across six sequencing cycles. (Right) magnified view of organelle staining of a representative cell. **(C)** Diffusion map embeddings of cell-cycle stage clusters determined using the single-cell expression profile for STARmap (upper left) and RIBOmap (upper right)

measurements along with corresponding protein fluorescence profiles of the FUCCI cell-cycle markers (STARmap, bottom left; RIBOmap, bottom right). **(D)** Single-cell translome covariation matrix showing the pairwise Pearson's correlation coefficients of the cell-to-cell variation, shown together with their averaged expression levels. Five strongly correlating blocks of coregulated translation modules (RTMs) are indicated by the gray boxes in the matrix, with RTMs 3 and 5 enlarged on the right. Cell cycle markers are highlighted in the enlarged matrix. **(E)** Matrix of the pairwise colocalization *P*-values describing the degree to which the reads of two genes tend to coexist in a sphere of a 3-μm radius in the same cell in RIBOmap results (left) and STARmap results (right), shown together with hierarchical clustering of these genes. The STARmap matrix uses the same order of genes as the RIBOmap matrix. Five

strongly correlating blocks of colocalized translation modules (LTMs) are indicated by the gray boxes in the matrix. (F) Bar plots visualizing the most significantly enriched gene ontology (GO) terms (maximum 3) in each of the five LTMs. (G) Enlarged gene matrix of LTMs 3 and 4. (H) A representative cell image showing the spatial distribution of RIBOmap signals of LTMs 3

and 4 genes, overlaid on the ER and cell boundary. (I) Quantification of the ER-localized percentage of genes of LTMs 3 and 4 versus all the detected genes. Wilcoxon signed-rank test, ***P < 0.0001. (J) The overlap percentage of LTM3 genes, LTM4 genes, and all 981 genes with ER-proximal RNAs identified by APEX-RIP.

fig. S8 A and B) and physically colocalize with ER staining (Fig. 3, H and I and fig. S8, D to F), suggesting they are ER-translated genes. Indeed, 62.2 and 94.6% of LTM4 genes overlapped with the proximity ribosome profiling dataset (8) and APEX-RIP dataset (33), respectively (Fig. 3J, fig. S8D, and table S4), suggesting the accuracy of RIBOmap for subcellular spatial analysis. By contrast, LTMs 1 and 3 are enriched for genes encoding large protein complexes of the mitotic spindle and translation machinery, respectively (Fig. 3, F and G, and fig. S8, A and C). This observation suggests that the subunits of large protein complexes may be synthesized in spatial proximity for efficient assembly. Finally, we explored whether coregulated genes tend to be colocalized for translation and found that the five RTMs also show strong subcellular colocalization (fig. S8G). These results may imply that functionally related gene groups can be coregulated through subcellular colocalized translation, possibly through shared regulatory RNA elements or protein–protein interactions between nascent proteins.

RIBOmap in intact mouse brain tissue

We then applied RIBOmap to mouse brain slices to reveal single-cell translatome profiles in intact tissues. We mapped a targeted gene list of 5413 genes (table S5) curated from previously published single-cell sequencing studies of mouse cell atlas (34–40). We imaged two biological replicates of the mouse hemisphere coronal sections (60,481 cells for Rep1 and 58,692 cells for Rep2) containing multiple brain regions (Fig. 4, A and B). We benchmarked tissue RIBOmap data by comparing the spatial translation pattern of well-known cell-type marker genes and neurotransmitter genes with corresponding *in situ* hybridization (ISH) images from the Allen Brain database (41) (Fig. 4C and fig. S9), where the comparison showed consistent spatial patterns. The data quality of RIBOmap is comparable to previous STARmap PLUS data (42) (fig. S10A). Notably, we observed a high correlation (Pearson $r = 0.95$) between the two RIBOmap replicates (fig. S10B), validating the reproducibility of RIBOmap.

Encouraged by the benchmarking results, we then adopted a hierarchical clustering strategy (20, 36) to identify cell types (fig. S10, C to E), resulting in 11 major cell types and 38 subtypes (Fig. 4, D and E, fig. S10, C to E, and fig. S11). The cross-reference analyses revealed good correspondence between RIBOmap cell clusters and published regional scRNA-seq

results of cell types (35) (fig. S10D). Based on these cell typing results, we generated spatial cell maps from the imaged hemibrain region (Fig. 4, F and G and fig. S12). This spatial cell-type map is consistent with previous reports (36), demonstrating the potential of RIBOmap single-cell translatomics to comprehensively identify diverse brain cell types and regions.

Cell type–specific and brain region–specific translational regulation in mouse brain

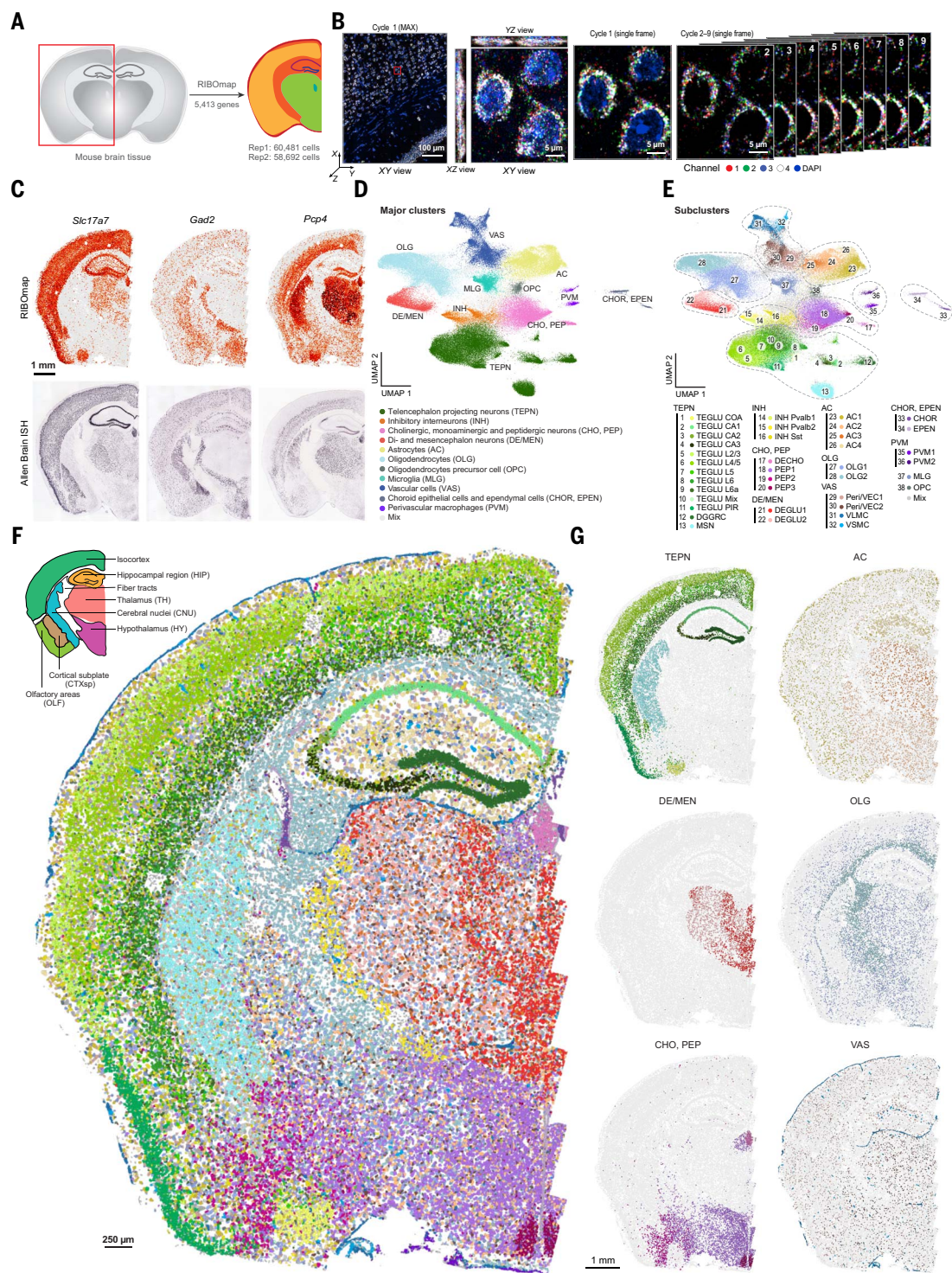
To compare the RIBOmap results with spatial transcriptomics, we conducted pairwise STARmap on a brain slice adjacent to RIBOmap sample followed by data integration for joint analyses (Fig. 5A). We observed consistent cell typing results between the two methods with respect to gene expression, cell-type composition, and spatial distribution of cell types (Fig. 5A and fig. S13). We also performed immunostaining of NeuN and GFAP proteins during RIBOmap and STARmap sample preparation and observed clear enrichment of NeuN protein signal in neurons and GFAP protein signal in astrocytes, respectively, in both samples (fig. S14), further supporting the accuracy of the cell typing results.

Leveraging the single-cell and spatial resolution of paired RIBOmap and STARmap data, we analyzed the heterogeneity of translational regulation across cell types and brain regions. We determined the reads correlation of 5413 genes between the two datasets for individual cell types or tissue regions (Fig. 5, B and C). Lower correlation scores indicate a greater degree of translational regulation, resulting in disparities between the translatome and the transcriptome. We found that non-neuronal cell types, especially oligodendrocytes, have lower correlation scores between translatome and transcriptome than neuronal cell types (Fig. 5B). Correspondingly, fiber tracts, the brain region where oligodendrocytes are enriched, had the lowest correlation (Pearson $r = 0.58$) between the translatome and transcriptome among the eight brain regions (Fig. 5C). This suggests a previously undercharacterized level of translational regulation in glial cells, particularly in oligodendrocytes.

To further pinpoint translationally regulated genes across various cell types, we performed gene clustering using major cell-type-resolved RIBOmap and STARmap profiles and identified 15 gene modules with distinct gene functions and expression patterns (fig. S15, A and

B, and table S6). Given that the oligodendrocyte lineage showed the lowest correlation between translatome and transcriptome among major cell types (Fig. 5C), we focused on gene modules that were highly expressed in oligodendrocyte lineage cells (240 genes; fig. S15A and table S6). Pseudotime trajectory analysis revealed the differentiation path of the oligodendrocyte lineage in our datasets (40), from oligodendrocyte precursor cells (OPC) to oligodendrocyte subtype 1 (OLG1), then to oligodendrocyte subtype 2 (OLG2) (Fig. 5, D and E). This is supported by the increased expression gradients of genes involved in myelination (*Plp1* and *Mbp*) along oligodendrocyte maturation (Fig. 5F) (43), and by the spatial enrichment of the more mature OLG2 in fiber tracts for myelination-based axon ensheathment (Fig. 5, G and H). To correlate translational regulation with oligodendrocyte subtypes and maturation, we further clustered oligodendrocyte-related gene modules using their subtype-resolved translatome and transcriptome profiles in the oligodendrocyte lineage (Fig. 5I, and table S6). We detected three gene modules: Module 1 and Module 2 have consistent patterns between RIBOmap and STARmap with the highest signals in OPC and OLG2 for most genes, respectively, whereas Module 3 has the highest RIBOmap signal in OLG2 but the highest STARmap signal in OLG1 for most genes (Fig. 5I). This observation suggested strong translational regulation for genes in Module 3. We further calculated the relative translation efficiency (RTE) for each gene using their ratio of RIBOmap and STARmap signals and found that genes in Module 3 had higher RTE in OLG2 than OLG1 and OPC (Fig. 5I). GO analysis revealed that Module 3 genes are involved in myelin sheath (i.e., *Cldn11* and *Tspan2*) (Fig. 5, J and K). Spatial analysis of Module 3 RTE patterns and representative genes across brain regions also showed the highest RTE value in the fiber tracts, where OLG2 is enriched (Fig. 5, L to O, and fig. S16A). We experimentally verified one example gene *Cldn11* and found that Claudin 11 (the protein product of *Cldn11*) immunostaining correlated better with *Cldn11* RIBOmap signal than STARmap signal, validating the accuracy of the spatial translatomic pattern we observed (fig. S16, B to E). Overall, through the integrative analysis of RIBOmap and STARmap results in the mouse brain, we identified gene modules that are translationally regulated during the maturation of oligodendrocyte lineage cells across different brain regions. The enhanced translation efficiency of Module 3 genes in OLG2

Fig. 4. Spatially single-cell translomic profiling of 5413 genes in the mouse brain. (A) Diagram of the imaged mouse coronal hemibrain region (red box) for RIBOmap. (B) Representative images showing the measurements of localized translation of 5413 genes by RIBOmap in a mouse coronal hemibrain slice. (Left) Maximum intensity (MAX) projection of the first sequencing round, showing all five channels simultaneously. Red square, zoom region. (Middle) Magnified view of three cells showing the MAX projection view of the first sequencing round. (Right) Magnified view of three cells showing the spatial arrangement of amplicons in a single z-frame across nine sequencing rounds. (C) RIBOmap and Allen Brain ISH images (41) showing the expression patterns of the three cell-type marker genes in comparable coronal hemibrain sections. (D and E) Uniform manifold approximation and projection (UMAP) plot visualization of translational profiles of 119,173 cells collected from mouse coronal hemibrains. 11 major cell types (D) and 38 subtypes (E) were identified using Leiden clustering. Cells identified as mixed cells numbered 7559 (see Methods) and were excluded from the downstream analysis. (F) Representative spatial cell type atlas in the imaged coronal hemibrain region using the same color code as in (E). (G) The respective spatial cell maps of six major cell types in the imaged coronal hemibrain region using the same color code as in (E).



Downloaded from https://www.science.org at Peking University on June 04, 2024

suggests substantial translation remodeling. This may functionally serve to augment the protein production for axon ensheathment and may be mechanistically relevant to the recent report on altered tRNA modification during oligodendrocyte maturation (44).

To systematically uncover genes with differential spatial patterns between translome and transcriptome across brain regions,

we performed gene clustering using region-resolved RIBOmap and STARmap profiles and identified gene modules with distinct spatial patterns between RIBOmap and STARmap across different brain regions (e.g., Module 7, fig. S17, A to C, and table S6). For example, G protein subunit gamma 2 (*Gng2*) in Module 7 has a low RIBOmap signal in the thalamus, which is consistent with the protein signal

(extracted from the HPA database) and less correlated with the STARmap signal (fig. S17, D to I). By contrast, the RNA ISH signals of *Gng2* from the Allen Brain database (41) correlated better with the STARmap signal than RIBOmap (fig. S17, J to M). These results were consistent with previous studies in which the translome is better correlated with the proteome than the transcriptome (7, 11, 12).

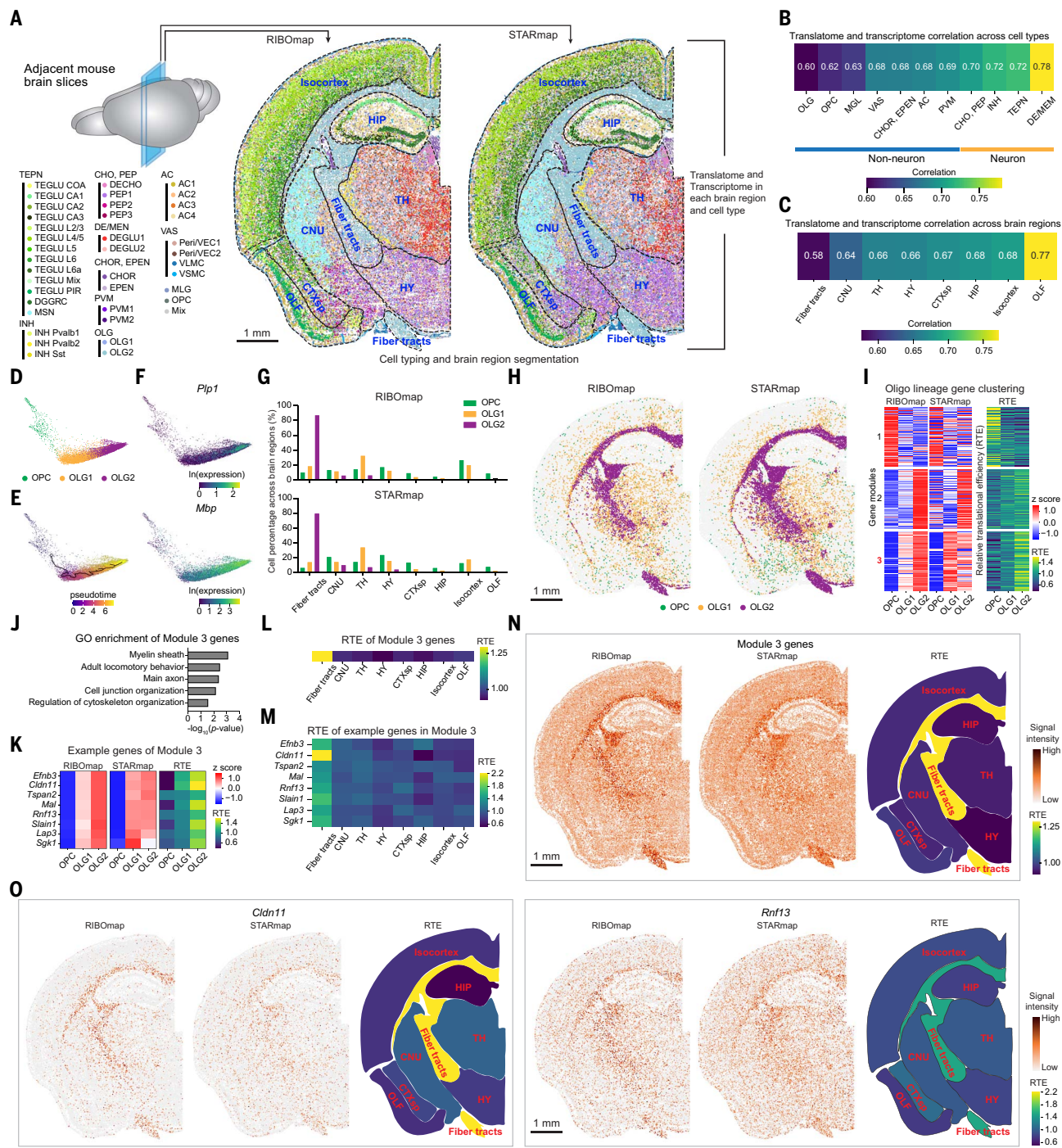


Fig. 5. Comparison of spatial translatome and transcriptome in the mouse brain. (A) Two adjacent mouse brain coronal sections were used for generating the spatial cell-type map. (B and C) The correlation of the translatome and transcriptome of the 5413 genes in each cell type (B) and brain region (C). (D) Diffusion map visualization of oligodendrocyte and OPC in RIBOmap samples. (E) Diffusion map with pseudotime trajectory visualization of oligodendrocyte and OPC in RIBOmap sample generated by Monocle 3. (F) Diffusion map showing the normalized expression level of oligodendrocyte lineage marker genes *Plp1* and *Mbp* in oligodendrocytes and OPCs. (G) Cell percentage of oligodendrocyte and OPC population in each brain region of RIBOmap (top) and STARmap (bottom) samples. (H) Cell-resolved spatial map for the oligodendrocyte and OPC population of RIBOmap (left) and STARmap (right) samples. (I) Heatmap showing the gene clustering using RIBOmap and STARmap results in the three oligodendrocyte lineage cell types (left) and the relative translational efficiency (RTE) of these genes in each oligodendrocyte lineage cell type (right). (J) The top 5 significantly enriched GO terms for Module 3 genes. (K) Heatmap showing the RIBOmap results (left), STARmap results (middle), and RTE (right) of example genes in Module 3. (L and M) Heatmap showing the average RTE values of all Module 3 genes (L) and the RTE value of Module 3 example genes (M) in each brain region. (N and O) RIBOmap (left) and STARmap (middle) images show the translation and transcription levels of all Modules 3 genes (N) and two Module 3 example genes (O), respectively. Each dot in the images represents a cell and the dot color represents the expression level. (Right) Spatial map showing the average RTE of all Module 3 genes (N) and the RTE of two Module 3 example genes (O) in each brain region.

showing the gene clustering using RIBOmap and STARmap results in the three oligodendrocyte lineage cell types (left) and the relative translational efficiency (RTE) of these genes in each oligodendrocyte lineage cell type (right). (J) The top 5 significantly enriched GO terms for Module 3 genes. (K) Heatmap showing the RIBOmap results (left), STARmap results (middle), and RTE (right) of example genes in Module 3. (L and M) Heatmap showing the average RTE values of all Module 3 genes (L) and the RTE value of Module 3 example genes (M) in each brain region. (N and O) RIBOmap (left) and STARmap (middle) images show the translation and transcription levels of all Modules 3 genes (N) and two Module 3 example genes (O), respectively. Each dot in the images represents a cell and the dot color represents the expression level. (Right) Spatial map showing the average RTE of all Module 3 genes (N) and the RTE of two Module 3 example genes (O) in each brain region.

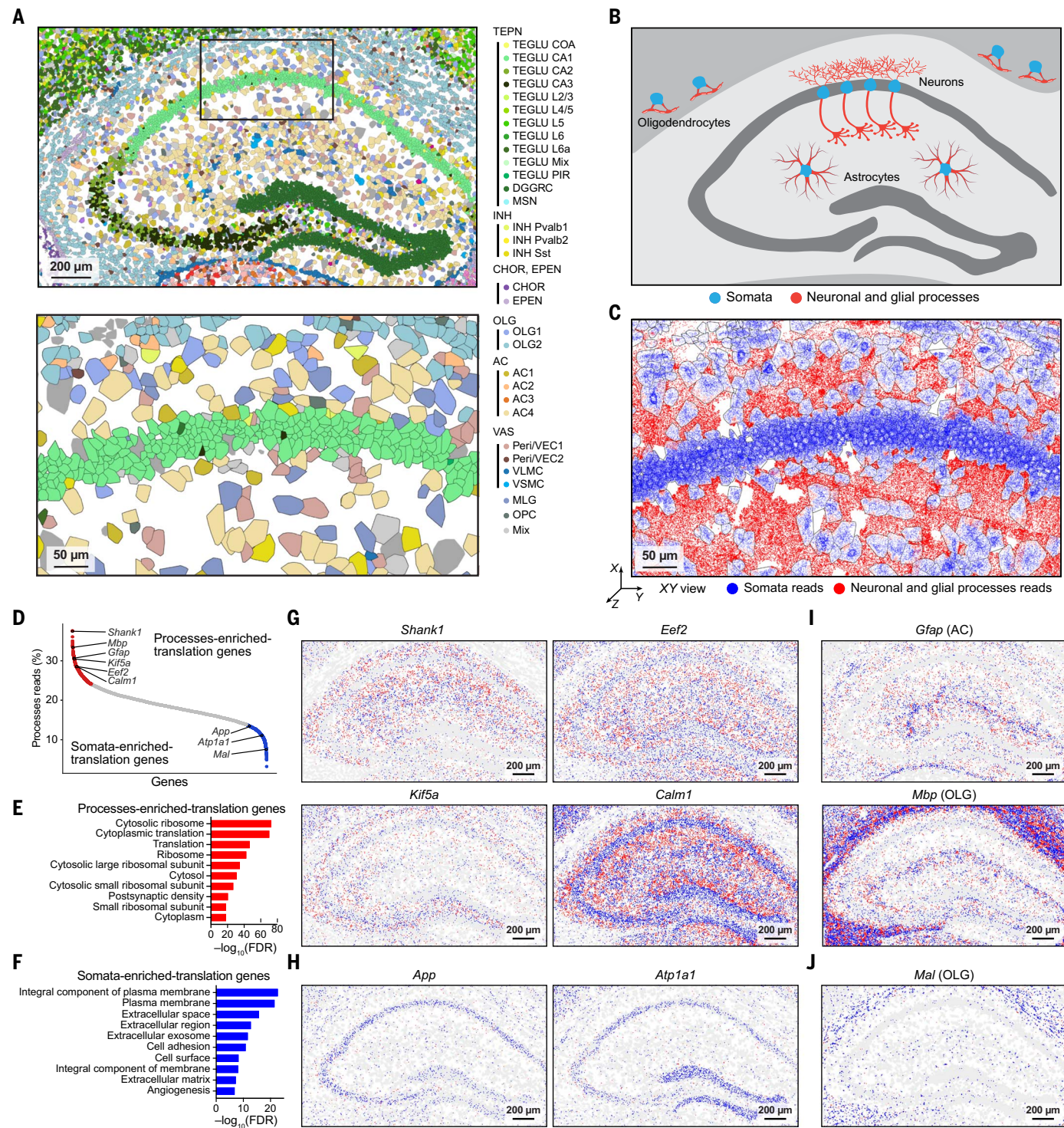


Fig. 6. Localized translation in the somata and processes of neuronal and glial cells in the mouse brain. (A) Magnified sections in the hippocampus and CA1 region showing the different cell types and the interspace. (B) Schematic of a hippocampal slice showing the somata and processes of hippocampal neurons, oligodendrocytes, and astrocytes. (C) Section in the CA1 region showing somata reads (blue) and neuronal and glial processes reads (red). (D) Processes read percentages of individual genes in the 5413-gene RIBOmap measurements, with genes rank-ordered based on their processes reads percentage. Nine example genes were labeled inset. (E) The top 10

significantly enriched GO terms for processes-enriched-translation genes. (F) The top 10 significantly enriched GO terms for somata-enriched translation genes. GO was analyzed by DAVID (see Methods). (G and H) The spatial translation map of representative processes-enriched translation genes (G) and somata-enriched translation genes (H) in the hippocampus, showing somata reads (blue) and processes reads (red). (I and J) The spatial translation map of glial cell marker genes, including examples of processes-enriched translation genes (I) and somata-enriched translation genes (J) in the hippocampus, showing somata reads (blue) and processes reads (red).

Subcellular localized mRNA translation in mouse brain

In addition to brain-wide anatomical analysis, we investigated potential translational control at the subcellular level. In the brain tissue, subcellular localized translation in the cell body (soma) and periphery branches (processes) serves as a critical mechanism to assemble and adjust the network of neuronal and glial cells (45–50) in response to physiological signals during neurodevelopment and memory. To dissect localized translation in the somata and processes of neuronal and glial cells, we divided the RIBOmap reads into somata reads (i.e., inside the cell body area identified by ClusterMap) (51) and processes reads (i.e., the rest of the reads) (Fig. 6, A to C). Next, we defined the top 10% of genes with the highest and lowest processes-to-somata ratios as processes- and somata-enriched translation genes, respectively (Fig. 6D and table S7). GO analysis showed that processes-enriched translation genes are associated with translation machinery and postsynaptic density (Fig. 6E and fig. S18A). By contrast, somata-enriched translation genes are associated with the plasma membrane and extracellular matrix (Fig. 6F and fig. S18B), corresponding to localized translation at the ER in the somata. Notably, we observed abundant processes-enriched translation signals in hippocampal neuropils (Fig. 6G and fig. S18C). By contrast, the somata-enriched translation genes showed sparse RIBOmap signals in hippocampal neuropils (Fig. 6H and fig. S18D), which may be associated with ER translation. Beyond neuronal genes, we also observed localized translation in glial cells (Fig. 6, I and J, and fig. S18, E and F). Overall, we demonstrated that RIBOmap can be used to study subcellular-localized translation in processes of both neuronal and glial cells of the mouse brain tissue.

In summary, RIBOmap is a spatial translomics method with single-cell and molecular resolution, which can be used to study mRNA regulation and protein synthesis in intact cellular and tissue networks. In contrast to existing approaches, RIBOmap bypasses complicated polysome isolation steps and genetic manipulation, thus holding promise for spatial and single-cell resolved studies in post hoc human tissue and disease samples. The detection efficiency and spatial resolution of RIBOmap can be further increased by combining with super-resolution imaging, expansion microscopy, and sparse labeling (52) to further illustrate translational events in fine subcellular structures (e.g., dissecting dendritic and axonic mRNA translation in neurons). It is noteworthy that the accuracy of RTE analysis depends on the precise joint cell typing of RIBOmap and STARmap data. Therefore, further computational development to improve the cross-modality integra-

tion of various spatial omics modalities will significantly enhance the analysis and interpretation of RIBOmap. Whereas RIBOmap in this manuscript focuses on mapping RNA translation, such proximity-based tri-probe design can be readily adapted to study RNA-RNA interactions, RNA-protein interactions, and RNA modifications. In the future, we envision that RIBOmap can be combined with other imaging-based measurements to enable spatial multiomics mapping of epigenome, transcriptome, and translatome in the same samples for an integrative understanding of biological systems.

REFERENCES AND NOTES

- J. A. Alfaro et al., The emerging landscape of single-molecule protein sequencing technologies. *Nat. Methods* **18**, 604–617 (2021). doi: [10.1038/s41592-021-01143-1](https://doi.org/10.1038/s41592-021-01143-1); pmid: [34099939](https://pubmed.ncbi.nlm.nih.gov/34099939/)
- T. Maier, M. Güell, L. Serrano, Correlation of mRNA and protein in complex biological samples. *FEBS Lett.* **583**, 3966–3973 (2009). doi: [10.1016/j.febslet.2009.10.036](https://doi.org/10.1016/j.febslet.2009.10.036); pmid: [19850042](https://pubmed.ncbi.nlm.nih.gov/19850042/)
- R. de Sousa Abreu, L. O. Penalva, E. M. Marcotte, C. Vogel, Global signatures of protein and mRNA expression levels. *Mol. Biosyst.* **5**, 1512–1526 (2009). doi: [10.1039/b908315d](https://doi.org/10.1039/b908315d); pmid: [20023718](https://pubmed.ncbi.nlm.nih.gov/20023718/)
- C. Vogel, E. M. Marcotte, Insights into the regulation of protein abundance from proteomic and transcriptomic analyses. *Nat. Rev. Genet.* **13**, 227–232 (2012). doi: [10.1038/nrg3185](https://doi.org/10.1038/nrg3185); pmid: [22411467](https://pubmed.ncbi.nlm.nih.gov/22411467/)
- B. Schwahnässer et al., Global quantification of mammalian gene expression control. *Nature* **473**, 337–342 (2011). doi: [10.1038/nature10098](https://doi.org/10.1038/nature10098); pmid: [21593866](https://pubmed.ncbi.nlm.nih.gov/21593866/)
- S. Das, M. Vera, V. Gandin, R. H. Singer, E. Tutucci, Intracellular mRNA transport and localized translation. *Nat. Rev. Mol. Cell Biol.* **22**, 483–504 (2021). doi: [10.1038/s41580-021-00356-8](https://doi.org/10.1038/s41580-021-00356-8); pmid: [3383730](https://pubmed.ncbi.nlm.nih.gov/3383730/)
- N. T. Ingolia, S. Ghaemmaghami, J. R. S. Newman, J. S. Weissman, Genome-wide analysis in vivo of translation with nucleotide resolution using ribosome profiling. *Science* **324**, 218–223 (2009). doi: [10.1126/science.1168978](https://doi.org/10.1126/science.1168978); pmid: [19213877](https://pubmed.ncbi.nlm.nih.gov/19213877/)
- C. H. Jan, C. C. Williams, J. S. Weissman, Principles of ER cotranslational translocation revealed by proximity-specific ribosome profiling. *Science* **346**, 1257521 (2014). doi: [10.1126/science.1257521](https://doi.org/10.1126/science.1257521); pmid: [25378630](https://pubmed.ncbi.nlm.nih.gov/25378630/)
- C. C. Williams, C. H. Jan, J. S. Weissman, Targeting and plasticity of mitochondrial proteins revealed by proximity-specific ribosome profiling. *Science* **346**, 748–751 (2014). doi: [10.1126/science.1257522](https://doi.org/10.1126/science.1257522); pmid: [25378625](https://pubmed.ncbi.nlm.nih.gov/25378625/)
- M. VanInsberghe, J. van den Berg, A. Andersson-Rolf, H. Clevers, A. van Oudenaarden, Single-cell Ribo-seq reveals cell cycle-dependent translational pausing. *Nature* **597**, 561–565 (2021). doi: [10.1038/s41586-021-03887-4](https://doi.org/10.1038/s41586-021-03887-4); pmid: [34497418](https://pubmed.ncbi.nlm.nih.gov/34497418/)
- N. T. Ingolia, Ribosome Footprint Profiling of Translation throughout the Genome. *Cell* **165**, 22–33 (2016). doi: [10.1016/j.cell.2016.02.066](https://doi.org/10.1016/j.cell.2016.02.066); pmid: [27015305](https://pubmed.ncbi.nlm.nih.gov/27015305/)
- Y. Liu, A. Beyer, R. Aebersold, On the Dependency of Cellular Protein Levels on mRNA Abundance. *Cell* **165**, 535–550 (2016). doi: [10.1016/j.cell.2016.03.014](https://doi.org/10.1016/j.cell.2016.03.014); pmid: [2704977](https://pubmed.ncbi.nlm.nih.gov/2704977/)
- J. M. Halstead et al., An RNA biosensor for imaging the first round of translation from single cells to living animals. *Science* **347**, 1367–1671 (2015). doi: [10.1126/science.aaa3380](https://doi.org/10.1126/science.aaa3380); pmid: [25792328](https://pubmed.ncbi.nlm.nih.gov/25792328/)
- B. Wu, C. Eliscovich, Y. J. Yoon, R. H. Singer, Translation dynamics of single mRNAs in live cells and neurons. *Science* **352**, 1430–1435 (2016). doi: [10.1126/science.aaf1084](https://doi.org/10.1126/science.aaf1084); pmid: [27131041](https://pubmed.ncbi.nlm.nih.gov/27131041/)
- T. Morisaki et al., Real-time quantification of single RNA translation dynamics in living cells. *Science* **352**, 1425–1429 (2016). doi: [10.1126/science.aaf0899](https://doi.org/10.1126/science.aaf0899); pmid: [27313040](https://pubmed.ncbi.nlm.nih.gov/27313040/)
- X. Yan, T. A. Hoek, R. D. Vale, M. E. Tanenbaum, Dynamics of Translation of Single mRNA Molecules In Vivo. *Cell* **165**, 976–989 (2016). doi: [10.1016/j.cell.2016.04.034](https://doi.org/10.1016/j.cell.2016.04.034); pmid: [27153498](https://pubmed.ncbi.nlm.nih.gov/27153498/)
- S. Boersma et al., Multi-Color Single-Molecule Imaging Uncovers Extensive Heterogeneity in mRNA Decoding. *Cell* **178**, 458–472.e19 (2019). doi: [10.1016/j.cell.2019.05.001](https://doi.org/10.1016/j.cell.2019.05.001); pmid: [3117819](https://pubmed.ncbi.nlm.nih.gov/3117819/)
- Z. B. Katz et al., Mapping translation ‘hot-spots’ in live cells by tracking single molecules of mRNA and ribosomes. *eLife* **5**, e10415 (2016). doi: [10.7554/eLife.10415](https://doi.org/10.7554/eLife.10415); pmid: [26760529](https://pubmed.ncbi.nlm.nih.gov/26760529/)
- S. tom Dieck et al., Direct visualization of newly synthesized target proteins *in situ*. *Nat. Methods* **12**, 411–414 (2015). doi: [10.1038/nmeth.3319](https://doi.org/10.1038/nmeth.3319); pmid: [25775042](https://pubmed.ncbi.nlm.nih.gov/25775042/)
- X. Wang et al., Three-dimensional intact-tissue sequencing of single-cell transcriptional states. *Science* **361**, eaat5691 (2018). doi: [10.1126/science.aat5691](https://doi.org/10.1126/science.aat5691); pmid: [29930089](https://pubmed.ncbi.nlm.nih.gov/29930089/)
- N. T. Ingolia, L. F. Larea, J. S. Weissman, Ribosome profiling of mouse embryonic stem cells reveals the complexity and dynamics of mammalian proteomes. *Cell* **147**, 789–802 (2011). doi: [10.1016/j.cell.2011.10.002](https://doi.org/10.1016/j.cell.2011.10.002); pmid: [22056041](https://pubmed.ncbi.nlm.nih.gov/22056041/)
- M. Clamer et al., Active Ribosome Profiling with RiboLace. *Cell Rep.* **25**, 1097–1108.e5 (2018). doi: [10.1016/j.celrep.2018.09.084](https://doi.org/10.1016/j.celrep.2018.09.084); pmid: [30355487](https://pubmed.ncbi.nlm.nih.gov/30355487/)
- I. Tirosh et al., Dissecting the multicellular ecosystem of metastatic melanoma by single-cell RNA-seq. *Science* **352**, 189–196 (2016). doi: [10.1126/science.aad0501](https://doi.org/10.1126/science.aad0501); pmid: [27124452](https://pubmed.ncbi.nlm.nih.gov/27124452/)
- F. M. Fazal et al., Atlas of Subcellular RNA Localization Revealed by APEX-Seq. *Cell* **178**, 473–490.e26 (2019). doi: [10.1016/j.cell.2019.05.027](https://doi.org/10.1016/j.cell.2019.05.027); pmid: [31230715](https://pubmed.ncbi.nlm.nih.gov/31230715/)
- X. Wang et al., N6-methyladenosine-dependent regulation of messenger RNA stability. *Nature* **505**, 117–120 (2014). doi: [10.1038/nature12730](https://doi.org/10.1038/nature12730); pmid: [24284625](https://pubmed.ncbi.nlm.nih.gov/24284625/)
- H. Shi et al., YTHDF3 facilitates translation and decay of N6-methyladenosine-modified RNA. *Cell Res.* **27**, 315–328 (2017). doi: [10.1038/cr.2017.15](https://doi.org/10.1038/cr.2017.15); pmid: [28106072](https://pubmed.ncbi.nlm.nih.gov/28106072/)
- A. Sakae-Sawano et al., Visualizing spatiotemporal dynamics of multicellular cell-cycle progression. *Cell* **132**, 487–498 (2008). doi: [10.1016/j.cell.2007.12.033](https://doi.org/10.1016/j.cell.2007.12.033); pmid: [18267078](https://pubmed.ncbi.nlm.nih.gov/18267078/)
- S.-B. Koh et al., Quantitative FastFUCI assay defines cell cycle dynamics at single-cell level. *J. Cell Sci.* **jcs.195164** (2016). doi: [10.1242/jcs.195164](https://doi.org/10.1242/jcs.195164); pmid: [27888217](https://pubmed.ncbi.nlm.nih.gov/27888217/)
- T. Robin, A. Bairach, M. Müller, F. Lisacek, L. Lane, Large-Scale Reanalysis of Publicly Available HeLa Cell Proteomics Data in the Context of the Human Proteome Project. *J. Proteome Res.* **17**, 4160–4170 (2018). doi: [10.1021/acs.jproteome.8.b00392](https://doi.org/10.1021/acs.jproteome.8.b00392); pmid: [30175587](https://pubmed.ncbi.nlm.nih.gov/30175587/)
- Y. Lin et al., eIF3 Associates with 80S Ribosomes to Promote Translation Elongation, Mitochondrial Homeostasis, and Muscle Health. *Mol. Cell* **79**, 575–587.e7 (2020). doi: [10.1016/j.molcel.2020.06.003](https://doi.org/10.1016/j.molcel.2020.06.003); pmid: [32589965](https://pubmed.ncbi.nlm.nih.gov/32589965/)
- D. Mahdessian et al., Spatiotemporal dissection of the cell cycle with single-cell proteogenomics. *Nature* **590**, 649–654 (2021). doi: [10.1038/s41586-021-03232-9](https://doi.org/10.1038/s41586-021-03232-9); pmid: [33627808](https://pubmed.ncbi.nlm.nih.gov/33627808/)
- M. E. Tanenbaum, N. Stern-Ginossar, J. S. Weissman, R. D. Vale, Regulation of mRNA translation during mitosis. *eLife* **4**, e07957 (2015). doi: [10.7554/eLife.07957](https://doi.org/10.7554/eLife.07957); pmid: [26305499](https://pubmed.ncbi.nlm.nih.gov/26305499/)
- P. Kwaepublics, D. M. Sheehan, W. Mallard, J. L. Rinn, A. Y. Ting, Live-cell mapping of organelle-associated RNAs via proximity biotinylation combined with protein-RNA crosslinking. *eLife* **6**, e29224 (2017). doi: [10.7554/eLife.29224](https://doi.org/10.7554/eLife.29224); pmid: [29239719](https://pubmed.ncbi.nlm.nih.gov/29239719/)
- A. Saunders et al., Molecular Diversity and Specializations among the Cells of the Adult Mouse Brain. *Cell* **174**, 1015–1030.e16 (2018). doi: [10.1016/j.cell.2018.07.028](https://doi.org/10.1016/j.cell.2018.07.028); pmid: [30096299](https://pubmed.ncbi.nlm.nih.gov/30096299/)
- Z. Yao et al., A taxonomy of transcriptomic cell types across the isocortex and hippocampal formation. *Cell* **184**, 3222–3241.e26 (2021). doi: [10.1016/j.cell.2021.04.021](https://doi.org/10.1016/j.cell.2021.04.021); pmid: [34004146](https://pubmed.ncbi.nlm.nih.gov/34004146/)
- A. Zeisel et al., Molecular Architecture of the Mouse Nervous System. *Cell* **174**, 999–1014.e22 (2018). doi: [10.1016/j.cell.2018.06.021](https://doi.org/10.1016/j.cell.2018.06.021); pmid: [30096314](https://pubmed.ncbi.nlm.nih.gov/30096314/)
- Tabula Muris Consortium, Overall coordination, Logistical coordination, Organ collection and processing, Library preparation and sequencing, Computational data analysis, Cell type annotation, Writing group, Supplemental text writing group, Principal investigators, Single-cell transcriptomics of 20 mouse organs creates a Tabula Muris. *Nature* **562**, 367–372 (2018). doi: [10.1038/s41586-018-0590-4](https://doi.org/10.1038/s41586-018-0590-4)
- N. Almanzar et al., A single-cell transcriptomic atlas characterizes ageing tissues in the mouse. *Nature* **583**, 590–595 (2020). doi: [10.1038/s41586-020-2496-1](https://doi.org/10.1038/s41586-020-2496-1); pmid: [3266974](https://pubmed.ncbi.nlm.nih.gov/3266974/)
- X. Han et al., Mapping the Mouse Cell Atlas by Microwell-Seq. *Cell* **173**, 1307 (2018). doi: [10.1016/j.cell.2018.05.012](https://doi.org/10.1016/j.cell.2018.05.012); pmid: [29775597](https://pubmed.ncbi.nlm.nih.gov/29775597/)
- J. Cao et al., The single-cell transcriptional landscape of mammalian organogenesis. *Nature* **566**, 496–502 (2019). doi: [10.1038/s41586-019-0969-x](https://doi.org/10.1038/s41586-019-0969-x); pmid: [30787437](https://pubmed.ncbi.nlm.nih.gov/30787437/)

41. E. S. Lein *et al.*, Genome-wide atlas of gene expression in the adult mouse brain. *Nature* **445**, 168–176 (2007). doi: [10.1038/nature05453](https://doi.org/10.1038/nature05453); pmid: [17151600](https://pubmed.ncbi.nlm.nih.gov/17151600/)
42. H. Zeng *et al.*, Integrative *in situ* mapping of single-cell transcriptional states and tissue histopathology in a mouse model of Alzheimer's disease. *Nat. Neurosci.* **26**, 430–446 (2023). doi: [10.1038/s41593-022-01251-x](https://doi.org/10.1038/s41593-022-01251-x); pmid: [36732642](https://pubmed.ncbi.nlm.nih.gov/36732642/)
43. S. Marques *et al.*, Oligodendrocyte heterogeneity in the mouse juvenile and adult central nervous system. *Science* **352**, 1326–1329 (2016). doi: [10.1126/science.aaf6463](https://doi.org/10.1126/science.aaf6463); pmid: [27284195](https://pubmed.ncbi.nlm.nih.gov/27284195/)
44. S. Martin *et al.*, Oligodendrocyte differentiation alters tRNA modifications and codon optimality-mediated mRNA decay. *Nat. Commun.* **13**, 5003 (2022). doi: [10.1038/s41467-022-32766-3](https://doi.org/10.1038/s41467-022-32766-3); pmid: [36008413](https://pubmed.ncbi.nlm.nih.gov/36008413/)
45. M. S. Fernandopulle, J. Lippincott-Schwartz, M. E. Ward, RNA transport and local translation in neurodevelopmental and neurodegenerative disease. *Nat. Neurosci.* **24**, 622–632 (2021). doi: [10.1038/s41593-020-00785-2](https://doi.org/10.1038/s41593-020-00785-2); pmid: [33510479](https://pubmed.ncbi.nlm.nih.gov/33510479/)
46. A. Biever *et al.*, Monosomes actively translate synaptic mRNAs in neuronal processes. *Science* **367**, eay4991 (2020). doi: [10.1126/science.ayy4991](https://doi.org/10.1126/science.ayy4991); pmid: [32001627](https://pubmed.ncbi.nlm.nih.gov/32001627/)
47. C. Glock *et al.*, The translatome of neuronal cell bodies, dendrites, and axons. *Proc. Natl. Acad. Sci. U.S.A.* **118**, e2113929118 (2021). doi: [10.1073/pnas.2113929118](https://doi.org/10.1073/pnas.2113929118); pmid: [34670838](https://pubmed.ncbi.nlm.nih.gov/34670838/)
48. L. M. Meservey, V. V. Topkar, M.-M. Fu, mRNA Transport and Local Translation in Glia. *Trends Cell Biol.* **31**, 419–423 (2021). doi: [10.1016/j.tcb.2021.03.006](https://doi.org/10.1016/j.tcb.2021.03.006); pmid: [33840591](https://pubmed.ncbi.nlm.nih.gov/33840591/)
49. K. Sakers *et al.*, Astrocytes locally translate transcripts in their peripheral processes. *Proc. Natl. Acad. Sci. U.S.A.* **114**, E3830–E3838 (2017). doi: [10.1073/pnas.1617782114](https://doi.org/10.1073/pnas.1617782114); pmid: [28439016](https://pubmed.ncbi.nlm.nih.gov/28439016/)
50. C. Müller, N. M. Bauer, I. Schäfer, R. White, Making myelin basic protein –from mRNA transport to localized translation. *Front. Cell. Neurosci.* **7**, (2013). doi: [10.3389/fncel.2013.00169](https://doi.org/10.3389/fncel.2013.00169)
51. Y. He *et al.*, ClusterMap for multi-scale clustering analysis of spatial gene expression. *Nat. Commun.* **12**, 5909 (2021). doi: [10.1038/s41467-021-26044-x](https://doi.org/10.1038/s41467-021-26044-x); pmid: [34625546](https://pubmed.ncbi.nlm.nih.gov/34625546/)
52. S. Alon *et al.*, Expansion sequencing: Spatially precise *in situ* transcriptomics in intact biological systems. *Science* **371**, eaax2656 (2021). doi: [10.1126/science.aaax2656](https://doi.org/10.1126/science.aaax2656); pmid: [33509999](https://pubmed.ncbi.nlm.nih.gov/33509999/)
53. H. Zeng *et al.*, Preprocessed dataset of the Spatially Resolved Single-cell Translatomics at Molecular Resolution, Version 1.0.1, Zenodo (2023); <https://zenodo.org/record/8041323>
54. H. Zeng *et al.*, Gene expression dataset of the Spatially Resolved Single-cell Translatomics at Molecular Resolution, Version 1.0.0, Zenodo (2023); <https://zenodo.org/record/8041114>
55. J. Huang, K. Wang, Z. Tang, J. Ren, H. Zeng, X. Wang, wanglab-broad/RIBOmap-analysis: v1.0.2, Version 1.0.2, Zenodo (2023); <https://zenodo.org/record/8041365>

ACKNOWLEDGMENTS

We thank S. Zhu (Broad Institute), M. Pan (Broad Institute) for technical assistance, J. Tian (Broad Institute), J. Liu (Harvard University), and L. Gaffney (Broad Institute) for helpful discussions and thoughtful comments on the manuscript. We thank F. Zhang (Broad Institute and MIT) for kindly providing the psPAX2 and VSVG plasmids. **Funding:** This work was funded by the following: The Searle Scholars Program (to X.W.); Thomas D. and Virginia W. Cabot Professorship (to X.W.); Edward Scolnick Professorship (to X.W.); Ono Pharma Breakthrough Science Initiative Award (to X.W.); Merkin Institute Fellowship (to X.W.); National Institutes of Health DP2 New Innovator Award 1DP2GM146245-01 (to X.W.); Helen Hay Whitney Foundation Postdoctoral Fellowship (to H.S.); and the National Institutes of Health Under Award T32AR007098 (to J.A.L.) X.W. acknowledges the support from the Searle Scholars Program, Thomas D. and Virginia W. Cabot Professorship, Edward Scolnick Professorship, Ono Pharma Breakthrough Science Initiative Award, Merkin Institute Fellowship, and NIH DP2 New Innovator Award. H.S. is supported by the Helen Hay Whitney Foundation Postdoctoral Fellowship. J.A.L. is supported by the NIH Under Award.

Author contributions: H.Ze., J.R., and X.W. optimized RIBOmap probe design and developed the method. H.Ze. performed RIBOmap experiments with the help of J.R., Y.Z., A.A., X.S., and H.C. J.H., C.K.W., Z.T., and H.Zh. performed computational analyses. H.Ze. prepared the FUCCI cell samples and Y.Z. prepared animal samples. H.Ze., J.H., C.K.W., and X.W. analyzed and interpreted the data with the inputs from Z.T., H.S., and J.A.L. All authors contributed to writing and revising the manuscript and approved the final version. X.W. conceptualized and supervised the project.

Competing interests: X.W., H.Z., and J.R. are inventors on pending patent applications related to RIBOmap. X.W. is a scientific cofounder of Stellaromics. All methods, protocols, and sequences are freely available to nonprofit institutions and investigators. **Data and**

materials availability: The RIBOmap preprocessed dataset and gene expression dataset are available on Zenodo ([53](https://zenodo.org/record/53), [54](https://zenodo.org/record/54)) and Single Cell Portal (SCP) (https://singlecell.broadinstitute.org/single_cell/study/SCP1835). All code and analysis are available on Zenodo ([55](https://zenodo.org/record/55)). Additional information is available at the Wang lab website (<https://www.wangxialab.org/>). **License information:** Copyright © 2023 the authors, some rights reserved; exclusive licensee American Association for the Advancement of Science. No claim to original US government works. <https://www.sciencemag.org/about/science-licenses-journal-article-reuse>

SUPPLEMENTARY MATERIALS

science.org/doi/10.1126/science.add3067

Materials and Methods

Figs. S1 to S18

Tables S1 to S7

References (56–69)

MDAR Reproducibility Checklist

[View/request a protocol for this paper from Bio-protocol.](https://www.jove.com/video/50000)

Submitted 2 June 2022; resubmitted 29 January 2023

Accepted 7 May 2023

10.1126/science.add3067